# Effect of Oxygen Flow Rate on PECVD Prepared ZnO Thin Films Physical Properties: Experiments Associated with DFT Calculations

S. Haireche[a,b,*], M. Bouchenafa[c,d], M.A. Fadla[e], A. Benmakhlouf[f], S. Maabed[c] and M. Sidoumou[d]

[a] *Laboratory of Physics of Experimental Techniques and Applications, University of Medea, Medea 26000, Algeria*
[b] *LASICOM Laboratory, Faculty of Sciences, University of Blida 1, Blida 09000, Algeria*
[c] *Department of Material Sciences, Faculty of Science, Amar Telidji University, BP 37G, Laghouat, 03000, Algeria*
[d] *Theoretical Physics and Radiation Matter Interaction Laboratory (LPTHIRM), University of Blida 1, 09000, Algeria*
[e] *Laboratoire de physique des matériaux, Université Amar Telidji de Laghouat, BP 37G Laghouat 03000, Algeria*
[f] *Laboratoire de Caractérisation et Valorisation des Ressources Naturelles, Université de Bordj Bou Arreridj, 34000, Algeria*

Received: 22.12.2021 & Accepted: 03.06.2022

Doi: 10.12693/APhysPolA.142.216 *e-mail: shaireche@outlook.fr

In this paper, we report on the deposition of zinc oxide thin films by the plasma enhanced chemical vapor deposition technique. The effects of oxygen flow rate on surface morphology, optic transmission, and gap energy are studied. The X-ray diffraction technique shows polycrystalline phases in the deposited material, the crystal structure is hexagonal, and the preferential orientation of crystal growth is in the (101) direction. The best optical transmission of zinc oxide is of the order of $\sim$ 89%, and a wide optical gap of $\sim$ 3.7 eV. To make a comparison with the present results and theoretical data, an *ab initio* calculation is carried out by the density functional theory method. To study the oxygen vacancies concentration effect on bandgap and optical transmission, we use three different configurations, namely $ZnO_{0.97}$, $ZnO_{0.94}$, and $ZnO_{0.91}$. To confirm our experimental and calculated results, we compared them to those given in the literature.

topics: zinc oxide, oxygen vacancies, PECVD, DFT

## 1. Introduction

Among the transparent conducting oxide (TCO) materials, zinc oxide thin films have been widely studied as transparent electrodes or hot plate sensors in many fields such as solar cells, gas sensors, flat panel displays, photocatalytic and biological applications, and transparent opto–electronic devices, due to their high transmittance and conductivity [1–10]. Among the major TCO materials, such as ZnO, $In_2O_3$, $SnO_2$, $TiO_2$, $CuAlO_2$, $CuInO_2$, $Cd_2SnO_4$, $InSbO_4$, $CdSnO_2$, etc, zinc oxide is very remarkable for its physical and chemical properties, in particular electrical and optical. The ZnO in the form of thin films is characterized by a low electrical resistivity of the order of $1–5\times10^{-4}$ $\Omega$ cm, a good optical transmission in the visible region ($\sim$90%), and a wide optical gap of 3.51 eV [1, 11]. Zinc oxide is easily obtained in the form of thin films by various crystal growth techniques such as pyrolysis spray [12–17], chemical vapor deposition (CVD) [18], magnetron sputtering [1, 11], pulsed laser deposition [19], sol–gel [15, 20–21], etc. Currently, ZnO is very competitive in multiple fields of the optoelectronic industry, and its electrical and optical properties are modified according to the field of application by doping with metallic elements (Cu, Mg, Ga, Ba, Co, Ni, Fe, In, Dy, etc) [1–3, 14, 19, 20, 22–24]. ZnO thin film is used as an anti-reflective layer to improve photovoltaic efficiency by reducing losses due to reflection phenomena. In addition, the incorporation of metallic elements in small amounts (few quantities) considerably improves the electrical sensitivity to the gas species [17].

Therefore, the control of the electrical and optical properties of thin films is a key parameter enabling the use of zinc oxide in various industrial fields.

The improvement in surface conductivity is related to oxygen deficits and doping concentrations of metallic elements. This improvement causes a decrease in optical transmission [14, 17]. Several works present the effect of the oxygen vacancy ($V_O$) on the photocatalytic activity and in adjusting the position of both the conduction and valence band. Indeed, Hongyan Liu et al. [25] investigated the effect of oxygen vacancy on the bandgap and showed that the bandgap increases with the decrease of oxygen partial pressure. Additional works [26–29] note the same trend. The bandgap is narrowed with the increase of oxygen vacancy concentrations, which is explained by the delocalized states in the valence band. Several experimental and theoretical works concerned obtaining high conductivity while maintaining good visible transmission. To achieve this, two research topics are launched in the present context. The first relates to optimizing the oxygen flow, reducing the resistivity at the surface while maintaining a good optical transmission [30]. The second is the search for new doping materials known as "light materials", conductivities of which vary according to doping while preserving good optical transmission [12, 20].

In this work, the important subject is in line with the first topic, which consists of the deposition and characterization of zinc oxide thin films with various oxygen flow rates by the plasma enhanced chemical vapor deposition (PECVD) technique. Indeed, we present in this work an original contribution to the improvement of the morphological and optical properties of zinc oxide by changing the oxygen flow rate. Optimization of the experimental parameters allowed us to obtain ZnO thin films of low surface resistivity verified by the good homogeneity of the surface and good optical transmission in the visible range. Moreover, the density functional theory (DFT) is also employed for computational study of $ZnO_x$. A zinc oxide with different supercell models $V_{O1}$, $V_{O2}$, and $V_{O3}$ is carried out to investigate the effect of oxygen vacancies on structural and electronic properties.

## 2. Experimental procedure

Zinc oxide thin films are deposited by PECVD (installed in PETA laboratory, Medea University). The process of the experimental device is shown in Fig. 1a. Plasma deposition apparatus usually consists of six modules or functions. Its main part is the reactor chamber, completed by the pumping system, power supply and monitor, electrical matching network, gases control system, and radio frequency (RF) plasma modulus. The most important part of the PECVD technique is the furnace reaching 1773 K, whose length is 100 cm. It consists of three segments (each 25 cm in length) separated by 5 cm in order to thermally insulate them from each other. During processing, an alumina tube ($Al_2O_3$) is inside the hollow cylinder of

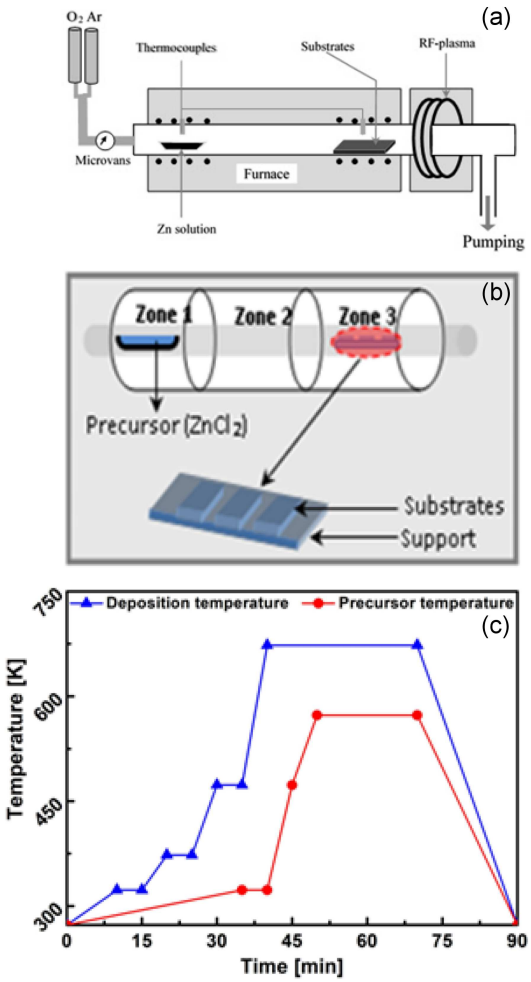


Fig. 1. (a) Experimental device of PECVD, (b) location of substrates and crucible holding the initial precursor $ZnCl_2$ in the reaction room (furnace), (c) heating diagram of the substrates and the precursor.

the furnace, which is used as a reaction chamber and transporter system for the gases. Continuous heating is maintained, provided by an input power until 6.6 kW. The heating at the level of the furnace is controlled by the heating diagram $T = f(t)$. The heating steps are performed automatically by the furnace, after programming the temperature in the 1st and 3rd furnace zones (Fig. 1c). Regarding the evaporation of the basic precursor containing $ZnCl_2$, we fixed the deposition temperature of the third zone at $T_d = 673$ K. We report that several trials were necessary to achieve such optimized experimental parameters. To control the oxygen flow rate, a module consisting of five microvalves is used to automatically control the entry of the various gases, like oxygen and argon, into the reaction chamber. Any change in the pressure inside the chamber is indicated by a pressure gauge. The PECVD has an RF generator, which generates plasma inside the reaction chamber with argon gas. The RF generator

provides ionizing discharge of the argon gas supplied with power radio frequencies of 500 W and frequency of 13.5 MHz. To reassure the quality and homogeneity of the ZnO thin films, a primary vacuum of the order of $10^{-3}$ Torr is launched into the reaction chamber.

The production of zinc oxide thin films is carried out on glass substrates of $15 \times 2 \times 25$ mm$^3$ with respect to the architecture of the reaction chamber as well as the different characterization techniques used in this work. The glass substrates were chosen because of the good agreement of thermal expansion coefficient between the glass substrate and zinc oxide ($\alpha_{\text{glass}} = 8.5 \times 10^{-6}$ k$^{-1}$ and $\alpha_{\text{ZnO}} = 6.5 \times 10^{-6}$ k$^{-1}$), to minimize constraints at the substrate-thin film interface, and for economic reasons. The cleaning of the substrates by chemical agents before the deposition of ZnO is necessary to remove impurities covering the substrate surface, such as dust, grease, organic impurities, etc. In a typical experiment, glass substrates are rinsed in concentrated hydrochloric acid (diluted at 20%), ethanol, acetone, and then deionized water in an ultrasonic cleaner for 10 min per step.

After cleaning and drying, the samples are arranged on the rack inside the furnace. The samples are placed on a support to prevent the deposit from occurring on both sides of the substrate. The substrates are placed in the 3rd zone of the furnace at ambient temperature and a primary vacuum (Fig. 1b). The deposition of zinc oxide thin films on glass substrates is performed using the solution consisting of two hydrated zinc dichloride ($ZnCl_2 + 2H_2O$) of 99.98% purity and ethanol. The zinc dichloride solution is prepared with ethanol at a temperature of 523 K for 5 min before allowing it to cool. The crucible holding the initial precursor $ZnCl_2$ is placed in the first zone of the furnace. The crystal growth of zinc oxide begins with the introduction of oxygen at a rate of 3, 6, and 9 sccm. When the vacuum in the reaction chamber reaches $10^{-3}$ Torr, the deposition temperature of the substrate stabilizes at 673 K, the evaporation temperature of $ZnCl_2$ reaches 573 K, and the deposition of ZnO is carried out for 10 min. In the 3rd zone of the furnace, where the substrates are kept, the reaction between the zinc in vapor form and oxygen takes place according to the following chemical reaction

$$ZnCl_2 + \frac{1}{2}O_2 \rightarrow ZnO + Cl_2. \quad (1)$$

The samples are kept under a primary vacuum for 30 min. After the deposition of the films, the samples were thermally treated at 523 K under an Argon flow rate of 20 sccm for 20 min. All experimental parameters were reported in Table I.

The microstructural properties of the prepared ZnO thin films are characterized by X-ray diffractometer Philips model using a copper cathode as the radiation source ($\lambda_1 = 1.540598$ Å and $\lambda_2 = 1.54439$ Å). The X-ray diffraction (XRD) spectra were acquired for $2\theta$ angles between 30 and 75°, with an angle of incidence of 1°. The step was fixed at 0.1°, and the counting time at 2 s per step. The surface morphology of the prepared ZnO thin films is characterized by atomic forces microscopy (A100 AFM from A.P.E. Research nanotechnology) in tapping mode. The spring constant of the cantilever was 0.6 N/m. The cantilevered tip oscillated close to the mechanical resonance frequency of the cantilever (typically 55–300 kHz) with amplitudes ranging from 10 to 50 nm. The transmittance spectra of the prepared ZnO thin films were determined by UV–VIS spectroscopy (UV-Vis 3000-SP nano spectrophotometry) in the 300–900 nm wavelength range.

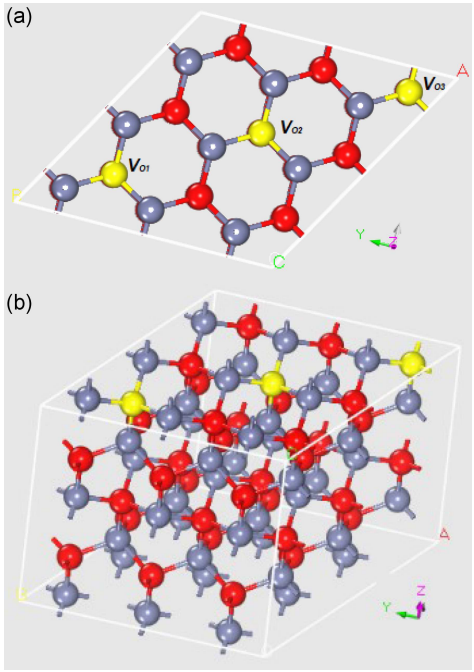


Fig. 2. Supercell ($3 \times 3 \times 2$) model with different oxygen vacancy sites terminology of stoichiometric $ZnO_x$ ($V_{O1}$ — first atom removing, $V_{O2}$ — second atom removing, $V_{O3}$ — third atoms removing).

TABLE I

Position parameters for zinc oxide thin films with PECVD.

| Experimental conditions | Value |
|---|---|
| $ZnCl_2$ powders | 5 g |
| Oxygen flow rate | 3, 6, 9 sccm |
| Argon flow rate | 20 sccm |
| Deposition time | 10 min |
| Deposition temperature | 673 K |
| Vacuum | $1.2 \times 10^{-3}$ Torr |
| RF-plasma frequency | 13.5 MHz |
| RF-plasma puissance | 300 W |
| Annealing time | 20 min |
| Annealing temperature | 523 K |

TABLE II

Comparative values of cell parameters $a$ and $c$, grains size ($d$), strain and dislocation density of zinc oxide.

| Cell parameters | | Grains size | Strain | Dislocation density | Ref. |
|---|---|---|---|---|---|
| $A$ [Å] | $c$ [Å] | $D$ [nm] | $\epsilon\ 10^{-3}$ | $\delta\ 10^{-3}$ [nm$^{-2}$] | |
| 3.030 | 5.186 | 15.4 | 2.300 | 4.21 | [this work] |
| 3.2483 | 5.2052 | 27.10 | 1.310 | 1.36 | [18] |
| 3.252 | 5.227 | 26.93 | 1.320 | 1.38 | [1] |
| 3.238 | 5.209 | 28.8 | 1.90 | 1.90 | [13] |
| 3.322 | 5.241 | 35.82 | 0.99 | 0.78 | [14] |
| 3.238 | 5.211 | 27.32 | 1.300 | 1.339 | [44] |
| 3.241 | 5.192 | 28.508 | 0.1216 | 1.23 | [16] |
| 3.008 | 5.212 | 19.25 | 0.886 | 2.70 | [45] |
| 3.23 | 5.23 | 15.3 | – | – | [43] |

## 3. Computational details and geometric models

The supercells $Zn_{36}O_{36-x}$, in which ($x = 1, 2, 3$), used in the calculation, were generated to remove one, two, and three oxygen atoms on the surface (Fig. 2). The removal of one atom ($V_{O1}$), two ($V_{O1,O2}$) and three ($V_{O1,O2,O3}$) oxygen ions, corresponds to atomic ratio O/Zn of 97.22%, 94.44%, and 91.66%, respectively in supercells (see Fig. 2). These ratios are comparable to that used in our experimental part.

First-principles calculation based on DFT with the plane-wave pseudo-potential method was performed using Cambridge Serial Total Energy Package (CASTEP) code [31]. Exchange and correlation effects were treated using the generalized gradient approximation of Perdew–Burke–Ernzerhof (GGA-PBE) [32, 33]. The pseudo-potential of Vanderbilt-type ultra-soft was used [34] within the following electronic valence states Zn ($3d, 4s$) and O ($2s, 2p$). Self-consistent calculations are considered to be converged when the total energy of the system is minimal. Thus, we have chosen the following convergence tolerance criteria: a total energy difference of less than $10^{-6}$ eV/atom, maximum ionic strength of Hellmann–Feynman of 0.01 eV/Å, and a maximum displacement of $5 \times 10^{-4}$ Å. The plane-wave energy of $E_{\mathrm{cut-off}} = 700$ eV and $12\times12\times6$ $K$-points mesh configuration were used after the convergence study.

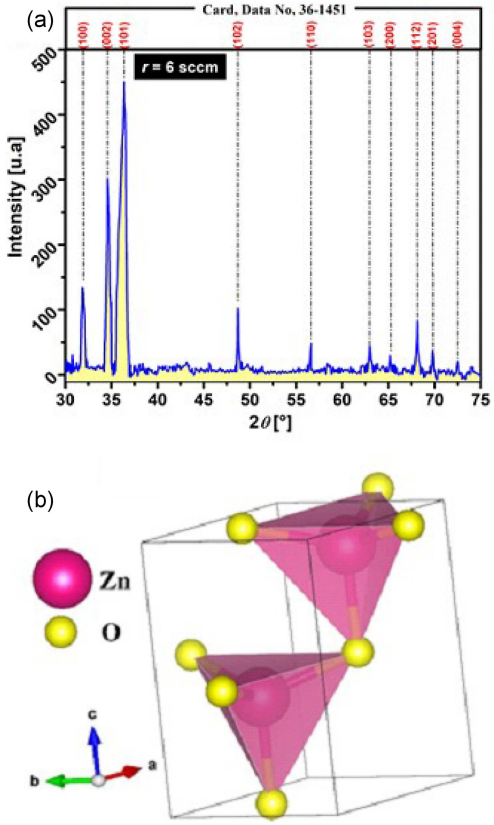


Fig. 3. (a) X-ray diffraction in $\theta$–$2\theta$ geometry of ZnO sample obtained with 6 sccm of oxygen flow rate. The top indexed diagram is for the undoped ZnO (JCPDS Card no. 36 — 1451). (b) Elementary unit cell of zinc oxide obtained by XRD.

## 4. Results and discussions

### 4.1. Structural properties

The XRD spectra of zinc oxide thin films deposited with 6 sccm oxygen flow rate are shown in Fig. 3a. The identification of all peaks from the XRD spectra makes it possible to demonstrate the existence of peaks representing the zinc oxide phase. The peaks are indexed in 31.82°: (100), 34.54°: (002), 36.42°: (101), 47.46°: (102), 56.74°: (110), 62.92°: (103), 66.06°: (200), 68.42°: (112), 69.06°: (201), and 73.82°: (004), respectively, based on the hexagonal (wurtzite) structure of ZnO with space group of $P_{63mc}$ and lattice parameters $a = b = 3.030$ Å, $c = 5.186$ Å and $\alpha = \beta = \pi/2$ and $\gamma = 2\pi/3$. The comparison of the lattice parameters shows that the deposited thin films crystallize

in the same crystal structure and present values of $a$ and $c$ close to those obtained by other experimental data and theoretical works, as shown in Table II. The primary unit cell of the zinc oxide obtained at a 6 sccm oxygen flow rate is shown in Fig. 3b.

The primary unit cell of the zinc oxide contains two atoms of zinc and three atoms of oxygen. Each zinc atom ($r_{Zn^{+2}} = 1.37$ Å) is the center of a trihedron formed by four oxygen atoms ($r_{O^{-2}} = 0.74$ Å). The positions of the oxygen atoms are given by: $(1/3, 2/3, 0)$, $(2/3, 1/3, 1/2)$, $(1/3, 2/3, 1)$, while zinc occupies positions $(1/3, 2/3, u)$ and $(2/3, 1/3, u + 1/2)$ such that $u = 0.381$. The predominant orientation obtained according to (101) coincides with the phase of zinc oxide represented in the reference data (Data no. 36 — 1451). Several experimental parameters affect the preferential orientation of zinc oxide thin films. The deposition technique, type of the precursor and its concentration, substrate nature, oxygen pressure, RF power, the nature and the concentration of doping, and the deposition temperature combine the parameters affecting the preferential orientation [1, 2, 35, 36]. J. Gregory [37] has shown that the predominant orientation changes from (002) to (100) when changing from the RF-sputter elaboration technique to the solution-film deposition technique. The nature of the initial precursor or its concentration also affects the predominant orientation [38]. Indeed, M. Tianlei [18] showed that the preferential orientation changes from (002) to (101) when the concentration of zinc acetate dihydrate increases from 0.05 to 0.25 mol./l. The appearance of the predominant orientation (004) when the deposition temperature is increased to 973 K, as in the work of R. Vinodkumar et al. [19], is generally linked to the activation energy, which depends on the fixing temperature of the zinc oxide molecules. In addition, doping with metallic elements (Al) changes the preferential orientation from (002) to (101), as has been shown in the works published by K. Khojier [3] and by E.A. Villegas et al. [12]. On the other hand, several works have reported that the preferential orientation does not change with Fe, In, Cu, and F elements doping, indicating that doping with these elements did not change the wurtzite ZnO structure, and that dopant substituted into the Zn sites [14, 20, 39]. Note that the change in the preferred orientation affects the morphology of the surface (grain size, shape, and grain boundaries). In the literature, the grain size is closely linked to preferential orientation, as shown in the study of S. Amirhaghi [40], who noticed a decrease in the size of the grains as a function of the increase in the deposition temperature and thickness of the thin films. These XRD peaks reveal the polycrystalline nature of ZnO deposited thin films. There is no diffraction peak for other phases like $ZnO_x$ observed in the XRD pattern, which concludes that Zn and O ions successfully consist in the lattice site. The crystal quality of the ZnO thin films is controlled by the crystallite size calculated from measurements on the peak in the diffraction pattern. The crystallites size ($D$) in the film was determined from the (101) preferential orientation using Scherrer's formula [41]

$$D = \frac{k\lambda}{\beta \cos(\theta)}, \tag{2}$$

where $k$ is constant (0.92 for the TCO materials), $\lambda$ is the X-ray wavelength, $\beta$ is the full width at half maximum (FWHM) of the XRD peak corresponding of the predominant orientation and $\theta$ is Bragg's diffraction angle. Therefore, we have established that the crystallites are of a nanometric scale can be used in magnetic applications [42, 43]. The lattice parameters of zinc oxide thin films are calculated using the following equation [13]

$$d_{hkl} = \left[\frac{4}{3}\left(\frac{h^2 + hk + k^2}{a^2}\right) + \left(\frac{l^2}{c^2}\right)\right]^{-\frac{1}{2}}, \tag{3}$$

where $h$, $k$, and $l$ are Miller indices, $d_{hkl}$ is the lattice spacings, and $a$ and $c$ are lattice parameters of the $a$-axis and $c$-axis, respectively. The reported results obtained for the lattice constant $a$ and $c$ are close to standard JCPDS values (Card. Data no. 36 — 1451) ($a = b = 3.25$ Å, $c = 5.20$ Å). The microstrain $\epsilon$ has been estimated using the following formula [11]

$$\varepsilon = \frac{k\lambda}{4D}, \tag{4}$$

where $\epsilon$ is the microstrain of the lattice in terms of the relative displacement of particles in the lattice, which excludes rigid body motions. This parameter allowed us to verify the required properties of the produced thin films. The dislocation density of the thin films $\delta$ is related to the crystallite size $D$ by the following equation [23]

$$\delta = \frac{1}{D^2}, \tag{5}$$

where $\delta$ is a linear crystallographic defect or irregularity within a crystal structure that contains an abrupt change in the arrangement of atoms. The number and arrangement of dislocations influence many properties of materials, such as the crystalline structure. From the XRD spectra, the values of cell parameters $a$ and $c$, the grain size $d$, the dislocation density $\delta$, and the microstrain $\epsilon$ are grouped and compared with other works [1, 13, 14, 16, 18, 43–45] in Table II.

The values of the cell parameters are in good agreement with those of the other works [45] with a weak deviation which is due to the experimental parameters and the deposition technique. Furthermore, as clearly shown in Table II, the calculated dislocation density is important when we compare it with other works [13, 14], probably due to the oxygen atoms occupation of interstitial sites and at the grain boundaries. In addition, we report that the grain size is similar to that in several experimental works [13, 14, 44] and in predictions in the theoretical study of M. Wu et al. [46].

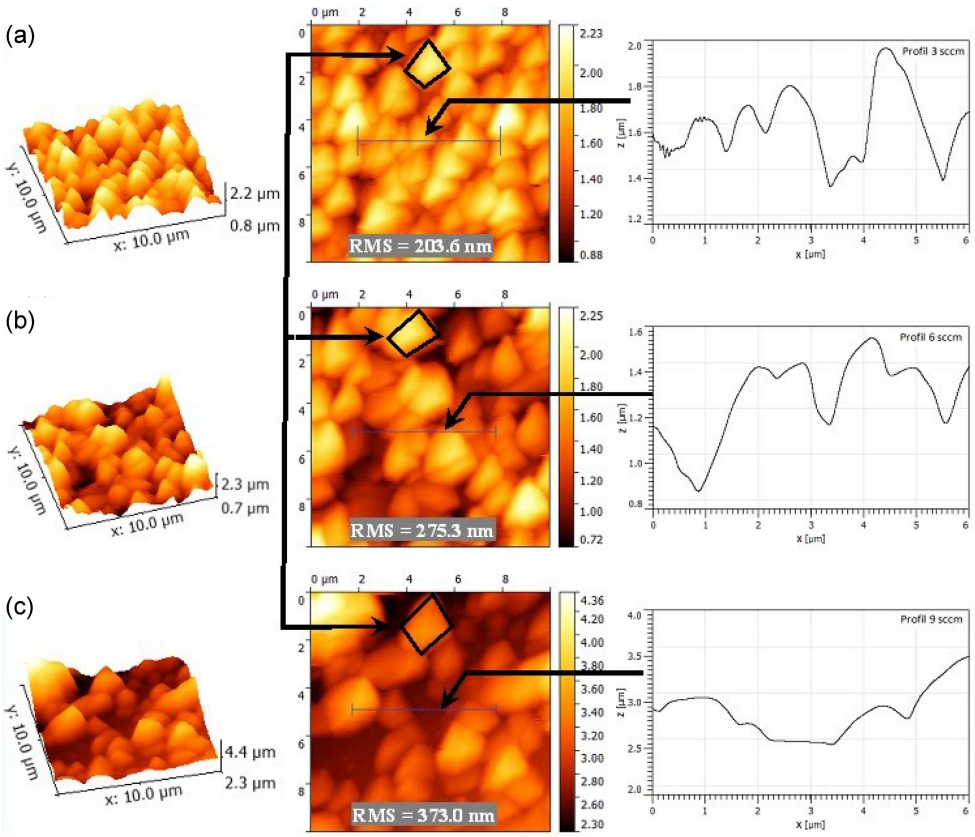


Fig. 4. AFM scans 3D, 2D and profile of ZnO with a variation of oxygen flow rate (a) 3 sccm, (b) 6 sccm and (c) 9 sccm.

### 4.2. AFM analysis

The surface morphology of zinc oxide thin films is obtained by atomic forces microscopy (AFM) under the effect of oxygen flow rate. In Fig. 4, we present the morphology of the surface in 2D and 3D, as well as the profile obtained with an oxygen flow rate of 3, 6, and 9 sccm. We have noticed in the different samples that the substrate is completely covered by dendrite-shaped islands. We found that the shape of the dendrites becomes more uniform and bigger as the oxygen flow rate is increased (see Fig. 4a–c at 2D). Additionally, we remark that the zinc oxide thin films obtained at 6 sccm have a similar orientation of the dendrites towards the hexagonal structure. We also remark a coalescence of the grains when we increase the oxygen flow rate from 3 to 9 sccm. We also notice that the average roughness of the zinc oxide surface increases considerably from 203.6 to 373.0 nm with the increase of oxygen flow rate from 3 to 9 sccm.

This variation is possibly due to the phenomena of grain coalescence when the incorporation of oxygen atoms in the matrix of zinc oxide is increased. Zinc oxide thin films produced with an oxygen flow rate of 9 sccm exhibit a high average roughness of the order of 373.0 nm according to Fig. 4. This high roughness is explained by the fact that the PECVD technique has a growth pattern according to Stranski–Krastanov [47]. In addition, the binding of ZnO molecules is strongly dependent on the reaction chamber geometry, the deposition temperature, and the formation energy.

### 4.3. Band structure

The band structure is among the electronic properties that can be obtained with Auger spectroscopy or numerical calculation methods (DFT, Hartree–Fock, etc) [46, 48–50]. The calculated band structures for zinc oxide without oxygen vacancies are presented in Fig. 5. The valence band and conduction bands are separated by a narrow zone of 0.80 eV. Both valence band maximum (VBM) and conduction band minimum (CBM) are located at the $\Gamma$ point, indicating a direct gap. It is well known that the theoretical gaps obtained by the GGA are approximately underestimated by about 30% [44].

To study the effect of $V_O$ concentration, we calculate the bandgap for three different configurations, namely $ZnO_{0.97}$, $ZnO_{0.94}$, and $ZnO_{0.91}$. Table III contains the different values of the gap calculated for the zinc oxide, with the experimental and theoretical data available in the literature [1, 15, 17–19, 23, 45, 51–55]. It is clear that the bandgap increases while the concentration of oxygen vacancy increases. The calculated gap values were 1.20, 1.45, and 1.88 eV for $ZnO_{0.97}$, $ZnO_{0.94}$,

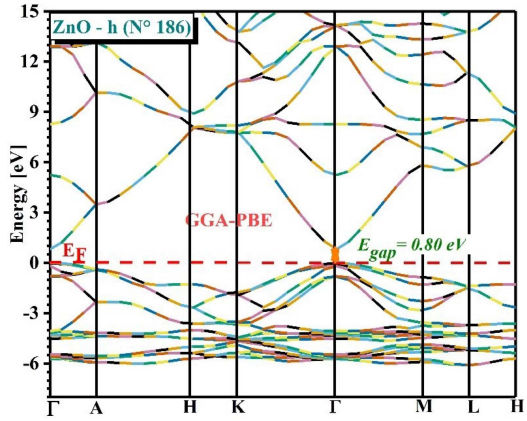


Fig. 5. The calculated electronic band structures of pristine ZnO.

TABLE III

Gap energy $E_g$ [eV] and transmission T [%] of zinc oxide thin films for sample obtained with 6 sccm compared with different elaboration methods and theoretical works.

| Method | | $E_g$ [eV] | T[%] | Refs |
|---|---|---|---|---|
| Our results | | | | |
| PECVD | | 3.78 | 80.2 | |
| DFT (GGA) | ZnO | 0.80 | – | |
| | $ZnO_{0.97}$ | 1.2 | – | |
| | $ZnO_{0.94}$ | 1.45 | – | |
| | $ZnO_{0.91}$ | 1.88 | – | |
| Experimental data | | | | |
| Magneton sputtering | | 3.375 | 80 | [1] |
| Sol–gel | | 3.24 | 90 | [15] |
| Spray pyrolysis | | 3.29 | 80 | [17] |
| AACVD | | 3.27 | 82.5 | [18] |
| Pulsed laser deposition | | 3.12 | 60 | [19] |
| Pneumatic spray | | 3.27 | 84 | [23] |
| RF sputtered | | 3.264 | 85–95 | [45] |
| Dip coating | | 3.29 | 50 | [52] |
| RF-PERTE system | | 3.27 | 80 | [53] |
| Other (theoretical) | | | | |
| DFT (GGA) | | 0.76 | – | [51] |
| | | 0.81 | – | [54] |
| | | 0.73 | – | [55] |
| DFT (GGA+U) | | 2.13 | – | [54] |

and $ZnO_{0.91}$ configurations, respectively. The values obtained by us are lower than those given experimentally by ≈ 39.6%. Compared to our experimental value of $E_g$ = 3.78 eV, the calculated bandgap was much smaller because of the well-known calculation error of Kohn–Sham DFT for the conduction band. However, these results did not affect the accuracy of the comparison between the different concentrations.

### 4.4. Density of states

The density of states (DOS) is an important quantity for calculating the energy distribution of electrons in the valence and conduction bands, which is required for a thorough understanding of several properties such as dielectric functions, transport properties, photoemission, etc [30, 51]. The calculated DOS is illustrated in Fig. 6, where the Fermi level is taken as the energy origin. The valence band, approximately −4 to 0 eV, is mainly dominated by the contribution of the $p_O$ state, with a small contribution from the overlap of the *sp* and *d* of Zn states. However, the maximum of valence band is formed by the states $d_{Zn}$ and $p_O$. The conduction region from approximately 0.8 eV is constituted by the *s* and *p* states of the Zn atom.

### 4.5. Optical properties

The study of optical properties consists in plotting the transmission spectra of zinc oxide thin films as a function of oxygen flow rate for 3, 6, and 9 sccm, as shown in Fig. 7. We have also performed *ab initio* calculation to compute transmission for $ZnO_{0.97}$, $ZnO_{0.94}$, and $ZnO_{0.91}$ configurations. Analysis of the transmission spectra shows that the zinc oxide thin films remain transparent in the visible range and opaque in the ultraviolet, depending on the variation of the oxygen flow rate.

We also noticed that the transmission of zinc oxide decreases with increasing oxygen flow rate. In fact, we obtained an average transmission coefficient of 89.4, 82.5, and 70.3% for oxygen flow rates of 3, 6, and 9 sccm, respectively (Table IV). This means that zinc oxide becomes more transparent in the visible range with decreasing oxygen flow rate. This trend can be interpreted in the following way.

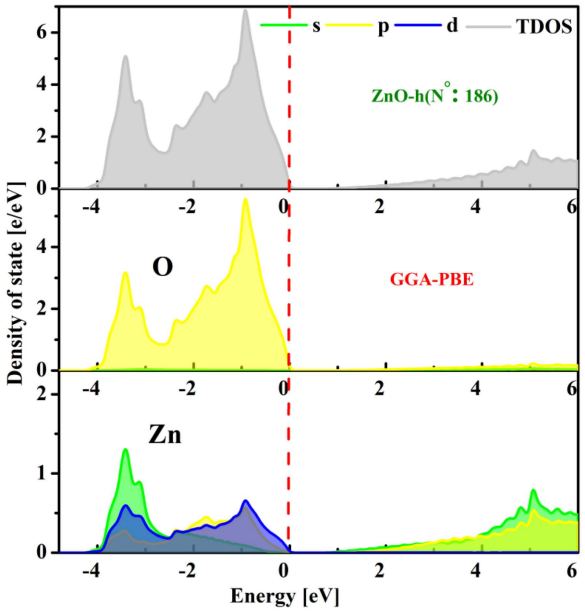


Fig. 6. Projected density of states PDOS and TDOS for ZnO compound.

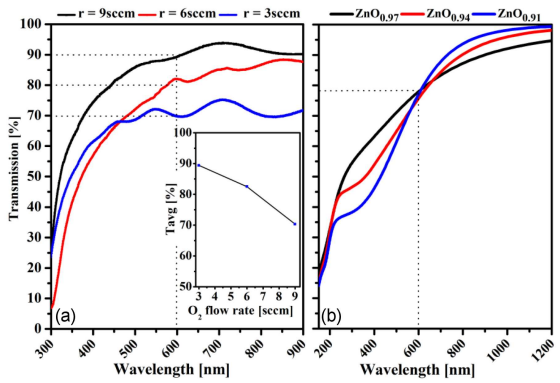


Fig. 7. Transmission spectra (a) ZnO thin film as a function of oxygen flow rate for 3, 6 and 9 sccm, (b) $Zn_{36}O_{36-x}$ supercells as a function of oxygen vacancies ($x = 1$, 2 and 3).

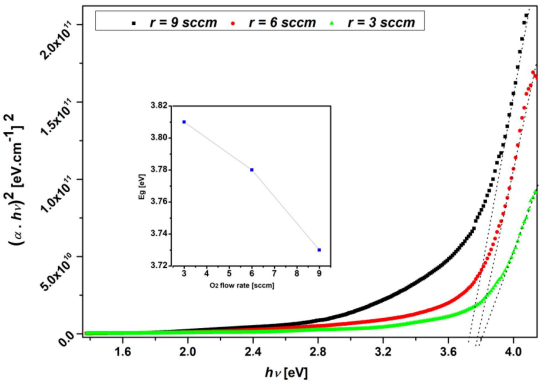


Fig. 8. The curves of $(\alpha h\nu)^2$ as a function of photon energy ($h\nu$) for ZnO thin films as a function of oxygen flow rate for 3, 6 and 9 sccm.

As the oxygen vacancy concentration rises, so does the bandgap of ZnO. We find that the decrease in the transmission is due to excess of oxygen at the surface. This behavior can be explained by the fact that oxygen takes up zinc sites by substitution. The average transmission of zinc oxide is compared with that in other experimental works in Table III. We remark that zinc oxide thin films have a better transmission value compared to that in other works [16, 17, 52]. This shows that zinc oxide is becoming a key material in the field of optoelectronics. On the other hand, through the transmission spectrum, we can also calculate the thickness of zinc oxide thin films. The thickness $d$ [nm] is calculated from the interference fringes appearing on the transmission spectrum in the visible range, using the method of Swanepoel [56] by the following formula

$$d = \frac{\lambda_1 \lambda_2}{2(n_1\lambda_2 - n_2\lambda_1)}, \tag{6}$$

where $\lambda_1$ and $\lambda_2$ represent the wavelengths [nm] corresponding to the two interference fringes and $n_1$ and $n_2$ are the refractive indices of thin films and air, respectively. The calculation which was made on the deposited samples according to the oxygen flow rate shows that the thickness varies slightly around of 192.15 nm with a relative uncertainty of 3.48%.

Using a transmission spectrum, we are able to determine a gap energy in the first Brillouin zone. The gap energy $E_g$ values of the ZnO thin films with different $O_2$ flow rates were obtained using Tauc's equation [57]

$$\alpha h\nu = A\,(h\nu - E_g)^{1/2}, \tag{7}$$

where $h\nu$ is the photon energy of the incident photons, $A$ is a constant, and $\alpha$ is the absorption coefficient. The absorption coefficient *alpha* can be determined from the transmission of the thin films with the formula $\alpha = (-1/d)\ln(T)$, where $d$ is the thickness of thin films. The value of the gap energy can be determined by extrapolation of the linear region of the plot of $(\alpha h\nu)^2$ versus photon energy ($h\nu$) on the $x$-axis. Figure 8 shows the relations between $(\alpha h\nu)^{1/2}$ and photon energy $h\nu$ for several oxygen flow rate values 3, 6, and 9 sccm.

TABLE IV

Average transmission $T_{avg}$ and gap energy us function of different values of oxygen flow rate. Note: average transmission value is obtained from the wavelength of 600 nm in the average of visible spectra (400–800 nm)

| $r$ [sccm] | $T_{avg}$ [%] | $E_g$ [eV] |
|---|---|---|
| 3 | 89.4 | 3.81 |
| 6 | 82.5 | 3.78 |
| 9 | 70.3 | 3.73 |

We also plot the gap energy as a function of oxygen flow rate. Figure 8 shows a variation of the gap energy from 3.81 to 3.73 eV obtained for an oxygen flow rate, which increases from 3 to 9 sccm. The decrease in gap energy with increasing oxygen flow may be due to excess oxygen atoms, which makes thin films more electrically conductive.

Previous works have noticed that there are several parameters, which affect the width of the forbidden band, such as the stress or dislocation density of the thin films, the doping with the metallic elements, the oxygen vacancies, as well as the presence of resistive phases in the ZnO thin films [1]. Our results show that two parameters affected the narrowing of the forbidden band, the dislocation density of thin films (Table II) and oxygen vacancies ($V_O$), since the resistive phases are absent according to the XRD analysis (Fig. 3a).

On the other hand, other studies have found that the oxygen deficit plays the opposite role [58]. Boroomand et al. [59] have shown that the gap energy remains constant by varying the oxygen flow rate. The values of $E_g$ are overestimated compared to experimental and theoretical papers [1, 15, 17–19, 23, 45, 51–55]. Analyzing the values of the gap energy represented in Table III,

we notice that they are comparable to each other. However, we find that zinc oxide obtained by low-cost techniques such as ours can give better optical properties such as gap energy or transmission.

## 5. Conclusion

In this work, we have deposited zinc oxide solid thin films on glass substrates by the PECVD technique for various oxygen flow rates. We have optimized the growth conditions with respect to the morphological and optical properties of our films. All the techniques used for the characterization were non-destructive so that measurements on the same sample could be done. The zinc oxide obtained in polycrystalline form and with a predominate orientation in the direction of (101) has a hexagonal structure with values of the lattice parameters, grain size, dislocation density, and strain with good agreement with the literature. Zinc oxide has a better optical transmission ($\sim 90\%$) and a wide optical gap of around $\sim 3.7$ eV for an oxygen flow rate of 6 sccm. From the microscopic study carried out by AFM, we have tried to give a description of the morphology of the surface. The morphological properties, such as grain size and surface roughness, are about 15.4 and 275.3 nm, respectively, for an oxygen flow rate of 6 sccm. Calculated results obtained from DFT show that the oxygen vacancy concentration has remarkable effects and can be used to adjust the bandgap as well as in optical transmission.

## Acknowledgments

The authors are grateful to Pr A. El Hdiy (ITheMM/EA7548), Université de Reims Champagne-Ardenne, Reims, France) and Pr A. Boufelfel (Laboratoire de physique, Université du 08 mai 45, Guelma 24000, Algeria) for valuable discussions. This work was supported by the Algerian Ministry of Higher Education and Scientific (MESRS) and the General Directorate of Scientific Research and Technological Development (DGRSDT).

## References

[1] Cong-sheng Tian, Xin-liang Chen, Jian Ni, Jie-ming Liu, De-kun Zhang, Qian Huang, Ying Zhao, Xiao-dan Zhang, *Solar Energy Mater. Solar Cells* **125**, 59 (2014).

[2] H. Zhu, J. Hüpkes, E. Bunte, S.M. Huang, *Appl. Surf. Sci.* **261**, 268 (2012).

[3] K. Khojier, *Mater. Sci. Semicond. Process.* **121**, 105283 (2021).

[4] Slimane Chala, Nouredine Sengouga, Fahrettin Yakuphanoglu, Saâd Rahmane, Madani Bdirina, Ibrahim Karteri, *Energy* **164**, 871 (2018).

[5] L.H. Kathwate, G. Umadevi, P.M. Kulal, P. Nagaraju, D.P. Dubal, A.K. Nanjundan, V.D. Mote, *Sensors and Actuat. A* **313**, 112193 (2020).

[6] W.C. Lim, J.P. Singh, Y. Kim, J. Song, K.H. Chae, T.-Y. Seong, *Vacuum* **183**, 109776 (2021).

[7] Gyeong-Beom Lee, Seung Hak Song, Myeong-Woo Lee, Yun-Jae Kim, Byoung-Ho Choi, *Appl. Surf. Sci.* **535**, 147731 (2021) .

[8] A. Paulson, N.A. Muhammed Sabeer, P.P. Pradyumnan, *Mater. Sci. Eng. B* **262**, 114745 (2020).

[9] T.K. Pathak, E. Coetsee-Hugo, H.C. Swart, C.W. Swart, R.E. Kroon, *Mater. Sci. Eng. B* **261**, 114780 (2020).

[10] M. Maache, T. Devers, A. Chala, *Semiconductors* **51**, 1604 (2017).

[11] Y. Andolsi, F. Chaabouni, *J. Alloys Compd.* **818**, 152739 (2020).

[12] E.A. Villegas, L.A. Ramajo, M.E. Lere, M.S. Castro, R. Parra, *Mater. Sci. Semicond. Process.* **121**, 105412 (2021).

[13] Aa.K. Ambedkar, M. Singh, V. Kumar, V. Kumar, B.P. Singh, A. Kumar, Y.K. Gautam, *Surf. Interfaces*, 19100504 (2020).

[14] B. Sahoo, K.J. Sankaran, R. Sakthivel, S. Kumar Pradhan, D. Behera, *Superlattices Microstruct.* **146**, 106666 (2020).

[15] C.-Y. Tsay, K.-S. Fan, S.-H. Chen, C.-H. Tsai, *J. Alloys Compd.* **495**, 126 (2010).

[16] K. Salim, M. Medles, A. Nakrela, R. Miloua, A. Bouzidi, R. Desfeux, *Optik* **210**, 164504 (2020).

[17] K.D.A. Kumar, S. Valanarasu, J.S. Ponraj, B.J. Fernandes, M. Shkir, S. AlFaify, P. Murahari, K. Ramesh, *J. Phys. Chem. Solids* **144**, 109513 (2020).

[18] T. Ma, *Mater. Sci. Semicond. Process.* **121**, 105413 (2021).

[19] R. Vinodkumar, I. Navas, K. Porsezian, V. Ganesan, N.V. Unnikrishnan, V.P.M. Pillai, *Spectrochim. Acta A Mol. Biomol. Spectrosc.* **118**, 724 (2014).

[20] T. Saidani, M. Zaabat, M.S. Aida, B. Boudine, *Superlattices Microstruct.* **88**, 315 (2015).

[21] X. Li, X. Zhu, K. Jin, D. Yang, *Opt. Mater.* **100**, 109657 (2020).

[22] B. Abdulkhair, M. Salih, A. Modwi, F. Adam, N. Elamin, M. Seydou, S. Rahali, *J. Mol. Struct.* **1223**, 128991 (2021).

[23] N. Guermat, W. Daranfed, I. Bouchama, N. Bouarissa, *J. Mol. Struct.* **51**, 129134 (2021).

[24] V.N. Jafarova, G.S. Orudzhev, S.S. Huseynova, V.R. Stempitsky, M.S. Baranava, *Semiconductors* **52**, 1047 (2018).

[25] H. Liu, F. Zeng, Y. Lin, G. Wang, F. Pan, *Appl. Phys. Lett.* **102**, 181908 (2013).

[26] S.A. Ansari, M.M. Khan, S. Kalathil, A. Nisar, J. Lee, M.H. Cho, *Nanoscale* **5**, 9238 (2013).

[27] C. Zhang, X. Geng, H. Liao, C.-J. Li, M. Debliquy, *Sensors Actuat. B Chem.* **242**, 102 (2017).

[28] J. Wang, R. Chen, L. Xiang, S. Komarneni, *Ceram. Int.* **44**, 7357 (2018).

[29] Y. Lv, W. Yao, X. Ma, C. Pan, R. Zong, Y. Zhu, *Catal. Sci. Technol.* **3**, 3136 (2013).

[30] A.A. Ziabari, S.J. Mousavi, M.H. Ahmadi, *Chin. J. Phys.* **57**, 61 (2019).

[31] M.D. Segall, P.J.D. Lindan, M.J. Probert, C.J. Pickard, P.J. Hasnip, S.J. Clark, M.C. Payne, *J. Phys. Condens. Matter* **14**, 2717 (2002).

[32] W. Kohn, L.J. Sham, *Phys. Rev.* **140**, A1133 (1965).

[33] J.P. Perdew, K. Burke, M. Ernzerhof, *Phys. Rev. Lett.* **77**, 3865 (1996).

[34] D. Vanderbilt, *Phys. Rev. B* **41**, 7892 (1990).

[35] Y.J. Kim, H.J. Kim, *Mater. Lett.* **21**, 351 (1994).

[36] A. Tanusevski, V. Georgieva, *Appl. Surf. Sci.* **256**, 5056 (2010).

[37] G.J. Exarhos, S.K. Sharma, *Thin Solid Films* **270**, 27 (1995).

[38] E.P. Zaretskaya, V.F. Gremenok, A.V. Semchenko, V.V. Sidsky, R.L. Juskenas, *Semiconductors* **49**, 1253 (2015).

[39] A. Sanchez-Juarez, A. Tiburcio-Silver, A. Ortiz, E.P. Zironi, J. Rickards, *Thin Solid Films* **333**, 196 (1998).

[40] S. Amirhaghi, V. Craciun, D. Craciun, J. Elders, I.W. Boyd, *Microelectron. Eng.* **25**, 321 (1994).

[41] W.L. Bragg, *Cryst. State* **1**, 189 (1946).

[42] Y. Larbah, M. Adnane, B. Rahal, *Semiconductors* **54**, 1439 (2020).

[43] N.S. Kumar, K.V. Bangera, G.K. Shivakumar, *Semiconductors* **49**, 899 (2015).

[44] A.S. Enigochitra, P. Perumal, C. Sanjeeviraja, D. Deivamani, M. Boomashri, *Superlattices Microstruct.* **90**, 313 (2016).

[45] N. Jain, R. Kumawat, S.K. Sharma, *Mater. Today Proc.* **30**, 93 (2020).

[46] M. Wu, D. Sun, C. Tan, X. Tian, Y. Huang, *Materials* **10**, 359 (2017).

[47] J.E. Prieto, I. Markov, *Surf. Sci.* **664**, 172 (2017).

[48] L.-C. Chao, S.-H. Yang, *Appl. Surf. Sci.* **253**, 7162 (2007).

[49] J. Wróbel, J. Piechota, *Solid State Commun.* **146**, 324 (2008).

[50] K. Harun, N.A. Salleh, B. Deghfel, M.K. Yaakob, A.A. Mohamad, *Results Phys.* **16**, 102829 (2020).

[51] P. Sikam, P. Moontragoon, Z. Ikonic, T. Kaewmaraya, P. Thongbai, *Appl. Surf. Sci.* **480**, 621 (2019).

[52] V. Balaprakash, M. Mohan, P. Gowrisankar, K. Thangavel, S. Sudha, *Mater. Today Proc.* **33**, 2251 (2020).

[53] G. Lavareda, P. Parreira, J. Valente, F.T. Nunes, A. Amaral, C.N. de Carvalho, *J. Non-Cryst. Solids* **356**, 1392 (2010).

[54] P. Palacios, K. Sánchez, P. Wahnón, *Thin Solid Films* **517**, 2448 (2009).

[55] J. Sołtys, J. Piechota, M. Łopuszyński, S. Krukowski, *J. Cryst. Growth* **374**, 53 (2013).

[56] R. Swanepoel, *J. Phys. E Sci. Instrum.* **16**, 1214 (1983).

[57] J. Tauc, R. Grigorovic, A. Vancu, *Phys. Status Solidi (b)* **15**, 627 (1966).

[58] S. Haireche, A. Boumeddiene, A. Guittoum, A. El Hdiy, A. Boufelfel, *Mater. Chem. Phys.* **139**, 871 (2013).

[59] B.B. Nasab, A. Kosarian, N.A. Sheini, *Semiconductors* **54**, 844 (2020).